Journal of Biomechanics 93 (2019) 52–59

Contents lists available at ScienceDirect

Journal of Biomechanics

journal homepage: www.elsevier.com/locate/jbiomech
www.JBiomech.com

Mapping the spatial variation of mitral valve elastic properties using air-pulse optical coherence elastography

Dragoslava P. Vekilov [a], Manmohan Singh [b], Salavat R. Aglyamov [c,d], Kirill V. Larin [b], K. Jane Grande-Allen [a,*]

[a] Rice University, Department of Bioengineering, Houston, TX, United States
[b] University of Houston, Department of Biomedical Engineering, Houston, TX, United States
[c] University of Houston, Department of Mechanical Engineering, Houston, TX, United States
[d] University of Texas at Austin, Department of Biomedical Engineering, Austin, TX, United States

ARTICLE INFO

Article history:
Accepted 14 June 2019

Keywords:
Mitral valve
Spatial pattern
Biomechanics
Optical coherence elastography

ABSTRACT

The mitral valve is a highly heterogeneous tissue composed of two leaflets, anterior and posterior, whose unique composition and regional differences in material properties are essential to overall valve function. While mitral valve mechanics have been studied for many decades, traditional testing methods limit the spatial resolution of measurements and can be destructive. Optical coherence elastography (OCE) is an emerging method for measuring viscoelastic properties of tissues in a noninvasive, nondestructive manner. In this study, we employed air-pulse OCE to measure the spatial variation in mitral valve elastic properties with micro-scale resolution at 1 mm increments along the radial length of the leaflets. We analyzed differences between the leaflets, as well as between regions of the valve. We found that the anterior leaflet has a higher elastic wave velocity, which is reported as a surrogate for stiffness, than the posterior leaflet, most notably at the annular edge of the sample. In addition, we found a spatial elastic gradient in the anterior leaflet, where the annular edge was found to have a greater elastic wave velocity than the free edge. This gradient was less pronounced in the posterior leaflet. These patterns were confirmed using established uniaxial tensile testing methods. Overall, the anterior leaflet was stiffer and had greater heterogeneity in its mechanical properties than the posterior leaflet. This study measures differences between the two mitral leaflets with greater resolution than previously feasible and demonstrates a method that may be suitable for assessing valve mechanics following repair or during the engineering of synthetic valve replacements.

1. Introduction

The mechanical behavior of heart valves is critical to their function and to overall cardiac health (Hinton and Yutzey, 2011). In the United States, approximately 2.5% of the population suffers from valvular heart disease, and 1.7% suffer specifically from mitral valve (MV) regurgitation, the backflow of blood from the left ventricle to the left atrium (Benjamin et al., 2019). Clinically, the two leaflets of the MV have dissimilar pathology, and the posterior leaflet (PL) is more often involved in disease than the anterior leaflet (AL) (Fedak et al., 2008; Grande-Allen et al., 2005). Surgical repair of the MV is the most common treatment of mitral regurgitation, and a broad range of devices have been developed to serve in this function. The annuloplasty ring is one such device that is inserted at the mitral annulus to relieve tension from the valve and help improve leaflet coaptation. This ring was originally flat and rigid in shape, but as studies revealed the mitral annulus to have a dynamic saddle-shaped configuration, the ring was redesigned to accommodate this natural geometry, thereby providing uniform annular force distribution, increasing leaflet coaptation, and improving the durability of repair (Bouma et al., 2015; Fedak et al., 2008; Jensen et al., 2008). The evolution of the annuloplasty ring illustrates the importance of considering region-specific properties in the study and treatment of MV disease, yet regional differences are often understudied or ignored entirely. Further, repair of the PL has higher long-term success with lower recurrent regurgitation than the AL (Gillinov et al., 1998; Spiegelstein et al., 2013). Differences in size, shape, composition, and structure between the two leaflets have been reported, but the particular reason for the discrepancy between presentation of disease and outcomes

* Corresponding author at: Rice University, Department of Bioengineering, 6100 Main St., MS 142, Houston, TX 77005, United States.
E-mail address: grande@rice.edu (K.J. Grande-Allen).

https://doi.org/10.1016/j.jbiomech.2019.06.015
0021-9290/

of repair for the leaflets is not well understood. Since the function of the MV involves dynamic mechanical stretch and depends upon its unique composition, understanding the heterogeneous structure and complex mechanical properties of the two leaflets is paramount to identifying underlying causes of disease and to improving repair techniques to ensure long-term success.

The MV is an anisotropic, viscoelastic tissue, whose two leaflets are each composed of four distinct tissue layers, including a collagen-rich fibrosa, glycosaminoglycan- (GAG) and proteoglycan- (PG) rich spongiosa, and elastin-rich atrialis and ventricularis. The AL is divided into clear and rough zones. The clear zone is adjacent to the annulus and lacks chordal insertions, thus making it uniformly thick, rigid, and smooth (Rabbah et al., 2013). The rough zone, which extends to the free edge, is thicker, but more pliable, and has uneven texture due to chordal insertions on the ventricular side. The PL does not have these distinct zones as it is entirely covered in chordal insertions. The unique layered structure of the MV allows different regions to withstand spatially-dependent forces as the valve opens and closes in response to cyclic pressure changes. Compared to the PL, the AL normally experiences higher stresses and has layers that vary in thickness throughout the leaflet (Kunzelman et al., 1993a, 1993b). Much of the thickness of the AL clear zone is due to the fibrosa layer, whereas the AL rough zone and the PL have a thicker spongiosa, which allows those regions to withstand repeated compressive stresses due to the leaflets' apposition during valve closure (Grande-Allen and Liao, 2011). These compositional differences translate to reported dissimilarities in the mechanical properties. The AL is stiffer and less extensible than the PL, and the AL clear zone has a higher tensile elastic modulus than the AL rough zone (May-Newman and Yin, 1995; Stephens et al., 2010). These differences are further propagated with age, with the mature adult AL exhibiting greater stiffness than its PL counterpart of the same age (Pham and Sun, 2014).

Although the mechanical properties of the leaflets have been previously reported (Barber et al., 2001; Grashow et al., 2006; May-Newman and Yin, 1995), the most established methods of mechanical testing, such as tension and compression testing, have important limitations. These methods are destructive, generally requiring leaflets to be cut into strips or small sections, and they depend on the assumption of consistent geometry and mechanical behavior throughout the test specimen. However, since the MV leaflets are known to be highly heterogeneous, such an assumption is limited at best. Various computational models have been developed to describe valve deformation and compute mechanical properties (Koch et al., 2010; Krishnamurthy et al., 2009; Kunzelman et al., 2007; Sacks and Yoganathan, 2007), but these methods are time consuming and similarly depend on numerous assumptions. An interesting study employed scanning acoustic microscopy to overcome some of these limitations to describe the distribution of mechanical properties along the leaflets (Jensen et al., 2006), but only three points on fixed ALs were examined and many questions were left unanswered about overall patterns of leaflet heterogeneity and differences between the two leaflets. Given the reported differences in composition, macro-scale biomechanical properties, and prevalence of pathological changes between the leaflets, there exists a need to better understand small-scale spatial patterns, so we can improve treatment of MV disease.

In this paper, we implement optical coherence elastography (OCE) to map out the elastic properties of intact MVs along their radial lengths. OCE is a nondestructive imaging technique that utilizes optical coherence tomography (OCT) (Huang et al., 1991) to image deformations in tissue (Larin and Sampson, 2017; Schmitt, 1998). Information about the deformation is then used to assess mechanical behavior. Unlike other mechanical testing methods, OCE is nondestructive because there is minimal mechanical loading of the material, it can be performed *in situ*, and it can detect micro-scale differences in elastic properties. OCE offers micrometer-scale spatial resolution with an imaging depth of ~1–2 mm and sub nanometer-scale displacement sensitivity, thus making it capable of accurately quantifying the mechanical properties of valve tissue. Employing OCE, we mapped out the spatial variation in elastic properties in MVs to assess differences between the two leaflets, as well as among leaflet regions.

2. Materials and methods

2.1. Sample preparation

MVs from young adult (6 month) and mature adult (2 years old) pigs were dissected from hearts purchased from a commercial abattoir (Animal Technologies, Tyler, TX). The ALs and PLs were separated from one another at the commissures. Chordae tendinae were removed by cutting as close to the leaflet as possible without damaging the leaflet to prevent confounding leaflet mechanics with those of the chordae. Leaflets were stored in phosphate buffered saline (PBS) at 4 °C until testing, for a maximum of two days.

2.2. Optical coherence elastography

Elastographic evaluation of the MV leaflets (n = 9 MVs, 5 young, 4 adult) was performed by OCE (Fig. 1A). A focused micro air-pulse induced a low amplitude deformation (<10 μm) in the MV leaflets, which then propagated as an elastic wave while imaged by an OCE system (Wang et al., 2013). Briefly, the OCE system was comprised of two major sub-systems: a phase-stabilized OCT system (Manapuram et al., 2009, 2008) and a focused micro air-pulse delivery system. The laser had a sweep rate of 30 kHz, central wavelength of ~1310 nm, and sweep range of ~150 nm. The axial and transverse resolutions of the system were ~11 μm and ~15 μm in air, respectively. The displacement stability of the system was ~20 nm in tissue.

OCE imaging was performed in M-B-mode, where the OCT probe beam was held stationary over time at a given position, and an elastic wave was induced by the air-pulse (Fig. 1C, Supplemental Movie 1) (Wang and Larin, 2014). The imaging was performed at 501 transverse lateral positions across the valve surface over an ~8 mm line, and the air-pulse was at the center of the scan. Each M-mode scan was 1500 samples, or 50 ms, long. The parameters were chosen based on our previous work (Wang and Larin, 2014) and to obtain a high-resolution image with sufficient spatial sampling. The raw phase data was converted to displacement and corrected for the motion of the surface and refractive index mismatch between air and the tissue (Song et al., 2013).

The elastic wave velocity was calculated based on a cross-correlation algorithm, as described in Fig. 2. The elastic wave propagation delays were determined by cross-correlation of vertical temporal displacement profiles with profiles from their corresponding excitation position. Then, the delays were linearly fitted to the corresponding propagation distances, and the velocity was determined from the slope. This procedure was repeated for each imaged in-depth layer. The cross-correlation analysis was performed on normalized displacement profiles, so any wave dampening did not affect the velocity calculation. While the elastic wave group velocity is related by a square root relationship to the sample elastic modulus (Graff, 2012), we have reported the elastic wave group velocities as a surrogate for stiffness as those are the values that were measured by OCE.

To characterize the spatial variation in biomechanical properties, 9–20 measurements were performed on each sample (Fig. 1A inset). The repeated measurements were taken at 1 mm

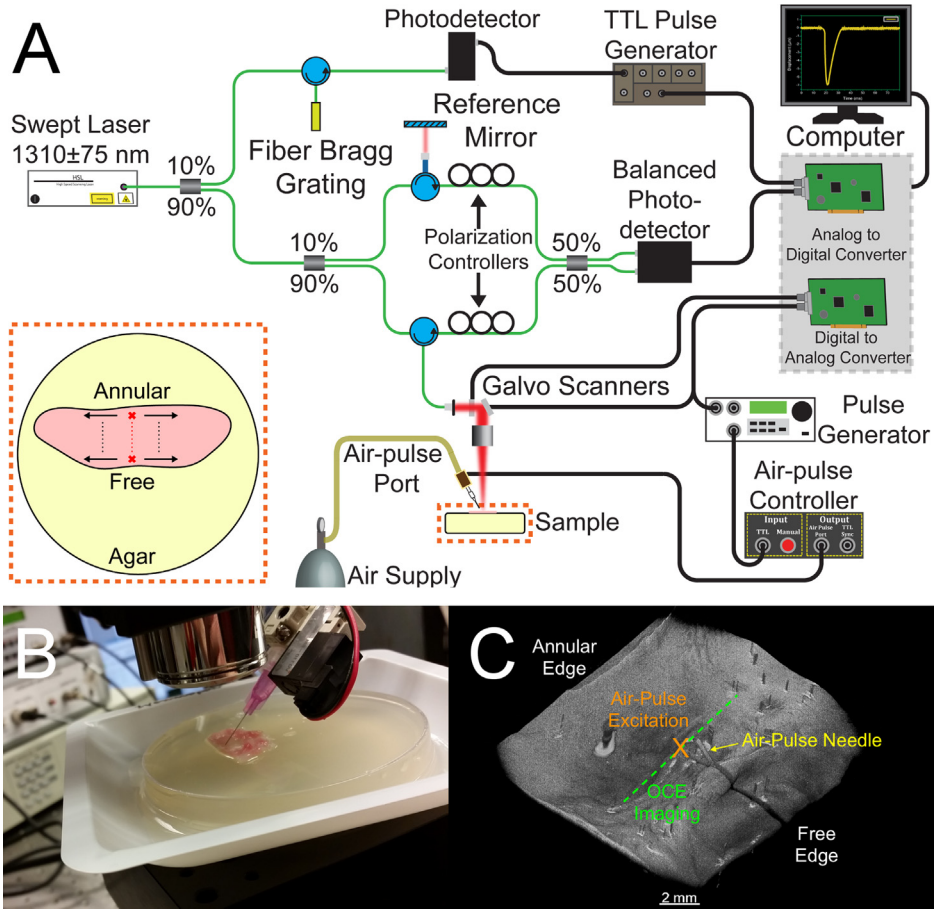

Fig. 1. (A) Schematic of the air-pulse OCE system and experimental setup. (Inset) Top-down view of the mitral valve leaflet on agar. The red X marks the location of the air puff delivery, and the black arrows represent the direction of wave propagation that is imaged by OCT. Measurements are taken along the radial length of the mitral leaflet, represented by dots between the two edges of the leaflets. (B) Photo of leaflet on agar set up for air puff delivery (needle) and OCT imaging lens. (C) 3D OCT image showing central location of air-puff delivery (orange X), which excites the tissue, and direction of subsequent OCE deformation measurement (green line) parallel to the annular edge. Video of this process can be found in Supplemental Movie 1. (For interpretation of the references to color in this figure legend, the reader is referred to the web version of this article.)

increments from the annular edge to the free edge with the collagen-rich fibrosa oriented upward. Due to the thin nature of the samples, the valve leaflets were placed on a 0.75% (w/w) agar basement (Fig. 1A and B) for stabilization during OCE imaging. To compare OCE trends to elastic moduli, uniaxial tensile testing was performed.

2.3. Spatial pattern analysis

Because the leaflets varied in length, differing numbers of measurements were taken per sample. To compare values between different size leaflets, positions were separated into 10 bins based on relative position from the annulus. The group velocities in each bin were averaged (±standard deviation) for each relative position for each leaflet. A limitation of this binning method is that each valve did not contribute an equal number of measurements to each bin. To confirm the pattern, each sample's positions were normalized from 0 to 1, and linear interpolation was used to calculate intermediate group velocities (Supplemental Fig. 1). Comparable results were acquired.

2.4. Uniaxial tensile testing

ALs and PLs were cut into strips for uniaxial mechanical testing (n = 11 MVs, 5 young, 6 adult). Circumferentially oriented annular, middle, and free edge sections 17 mm long and 4 mm wide were cut from the leaflets beginning at the annulus (Supplemental Fig. 2). Thickness, width, and the gauge length were measured prior to testing with an EnduraTEC ELF 3220 (Bose, Eden Prairie, MN). The test involved 20 triangle waves at 0.33 Hz of 2 mm displacement for preconditioning before a final stretch to failure at 0.1 mm/s. Raw load and displacement data was converted to stress-strain curves using tissue dimensions (Puperi, 2016). The elastic modulus was determined by finding the maximum slope of the bilinear stress-strain curve that covered at least 4% strain.

2.5. Statistical analysis

For the spatial pattern analysis, group velocities for each relative position were compared between the two leaflets using paired t-tests. For the regional analysis of OCE data, points for each sample leaflet were separated into three equal parts (annular, middle, and free edge). For both OCE and tensile testing data, two-way ANOVA with post hoc multiple comparisons test with Bonferroni correction was performed to assess differences between the three regions and the two leaflets. A three-way ANOVA was performed to assess differences between age groups, regions, and leaflets. The results were verified using a linear mixed model with the subject as a random effect and age, region, and leaflet as fixed effects. Differences were considered significant at $p < 0.05$ or a Bonferroni

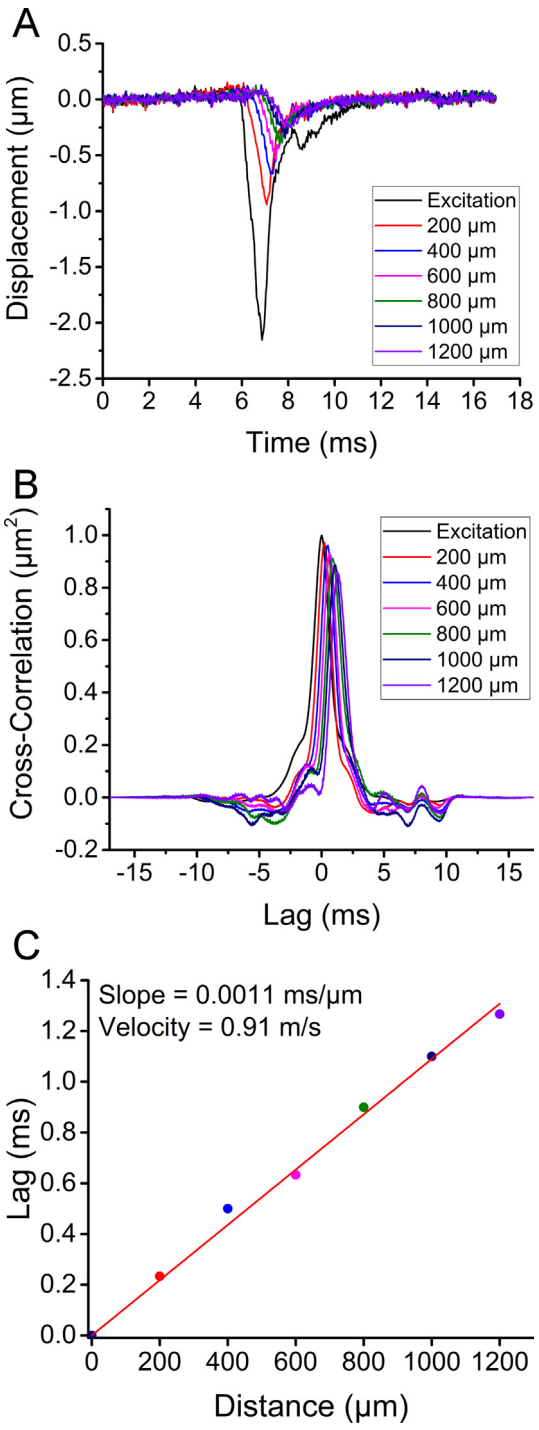

Fig. 2. Elastic wave group velocity calculation procedure. (A) Selected temporal displacement profiles from the surface of a typical leaflet at the indicated distances away from the air-pulse excitation are shown. (B) Cross-correlation analysis of the elastic wave propagation was used to calculate the wave propagation velocity. The displacement profiles at each of the distances away from the excitation, as shown in (A), were cross-correlated with the excitation displacement profile. The peak of the cross-correlation was selected as the wave propagation delay to that given position. (C) Linear fitting was used to calculate the elastic wave propagation velocity based on the elastic wave propagation delays as determined in (B) to the (color-coded) corresponding propagation distances. Since the wave propagation distances were known, the least squares regression fitting was used to minimize the error between the fit and the elastic wave propagation delay. Thus, the inverse of the slope was the wave velocity. (For interpretation of the references to color in this figure legend, the reader is referred to the web version of this article.)

corrected value for multiple comparisons of $p < 0.05/N$ where N was the number of comparisons. Bonferroni adjusted confidence intervals are reported. Graphs report mean ± standard deviation.

3. Results

3.1. Age-related differences

Our analysis did not detect any age-related differences. There were no statistically significant differences detected between the OCE-measured group velocity or elastic modulus measured by tensile testing (Supplemental Fig. 3). Because age-related differences were not detected, the remaining analyses considered all valves as a single group, independent of age.

3.2. Spatial variation

Using OCE, we have created the first point-by-point map of elasticity variation along the relative radial length of MV leaflets (Fig. 3A, Supplemental Table 1). The AL had a significantly greater

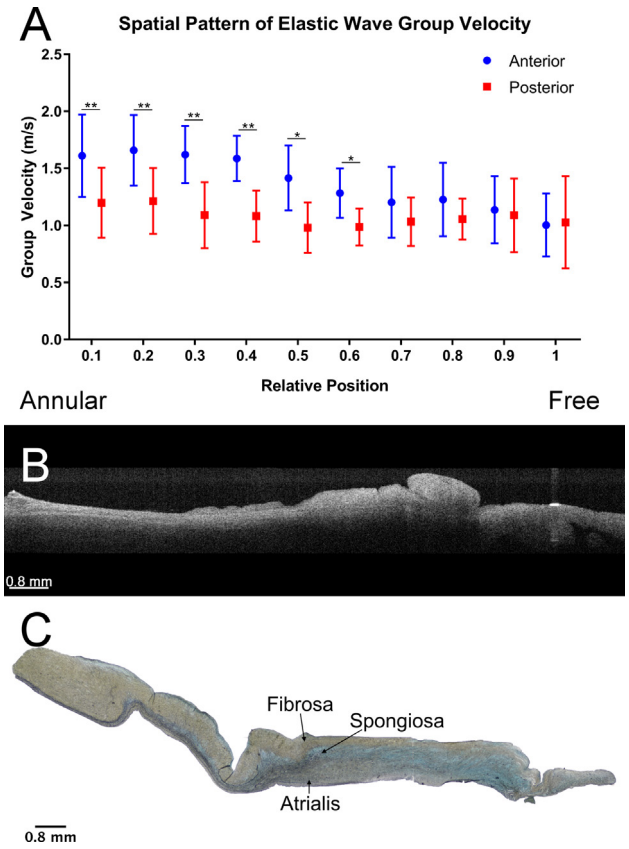

Fig. 3. (A) Mapping of the spatial elastic wave group velocity pattern acquired by OCE for anterior and posterior leaflets. Anterior leaflet had significantly greater group velocity, which is reported as a surrogate for stiffness, at positions 0.1–0.6, corresponding to 60% of the valve nearest the annular edge, than posterior leaflet. * = $p < 0.05$; ** = $p < 0.01$. (B) OCT image of mitral leaflet as imaged for OCE. (C) Movat pentachrome stain of mitral leaflet showing layered composition of yellow-stained collagen in fibrosa layer, blue-stained proteoglycans and glycosaminoglycans in spongiosa, and black-stained elastin in atrialis. In (B) and (C), the thick collagen-filled fibrosa layer is oriented upward, as was the leaflet during OCE analysis. In (A–C), the annular edge is on the left, aligning with position 0.1. (For interpretation of the references to color in this figure legend, the reader is referred to the web version of this article.)

group velocity at relative positions 0.1 through 0.6, corresponding to the 60% of the leaflet length nearest the annular edge, compared to the PL. Positions 0.7 through 1.0 were not significantly different between the two leaflets.

3.3. Anterior vs. posterior leaflet

Overall, the AL had a significantly greater group velocity than the PL (Anterior: 1.38 ± 0.17 m/s, Posterior: 1.07 ± 0.16 m/s, p = 0.0056, 95% CI: 0.15, 0.44 m/s; Fig. 4A). This pattern was evident in 5 of the 9 valves (Supplemental Fig. 4). When comparing the specific regions of the two leaflets, the annular edge and middle region of the AL had a significantly greater group velocity than the PL (Annular Anterior: 1.68 ± 0.20 m/s, Annular Posterior: 1.14 ± 0.26 m/s, p = 0.0006, 95% CI: 0.31, 0.77 m/s; Middle Anterior: 1.30 ± 0.22 m/s, Middle Posterior: 1.02 ± 0.16 m/s, p = 0.0120, 95% CI: 0.08, 0.48 m/s). At the free edge, however, there was no significant difference between the elastic wave velocity in ALs and PLs (Anterior: 1.08 ± 0.28 m/s, Posterior: 1.06 ± 0.28 m/s, 95% CI: −0.20, 0.30 m/s, p = 0.6488).

3.4. Regional analysis

When points for each sample leaflet were separated into annular, middle, and free edge regions (Supplemental Table 2), the overall group velocity of the annular edge was significantly greater than that of the both the middle and free edge (Annular: 1.41 ± 0.36 m/s; Middle: 1.16 ± 0.24, p = 0.0026, 95% CI: 0.09, 0.42 m/s; Free: 1.07 ± 0.27 m/s, p = 0.0017, 95% CI: 0.13, 0.24 m/s; Fig. 4B). No significant difference existed between the middle and free edge (p = 0.3050, 95% CI: −0.08, 0.23 m/s). The AL displayed a similar pattern, where the velocity was significantly greater in the annular edge compared to the middle and free edges, but there was no significant difference between the middle and free edge, albeit only marginally (Annular: 1.68 ± 0.20 m/s; Middle: 1.30 ± 0.22 m/s, p = 0.0040, 95% CI: 0.16, 0.60 m/s; Free: 1.08 ± 0.28 m/s, p = 0.0001, 95% CI: 0.38, 0.76 m/s; Middle vs. Free p = 0.048, 95% CI: 0.00, 0.47 m/s). However, no significant differences were evident in the PL (Annular: 1.14 ± 0.26 m/s; Middle: 1.02 ± 0.16 m/s, p = 0.2167, 95% CI: −0.09, 0.33 m/s; Free: 1.06 ± 0.28 m/s, p = 0.4494, 95% CI: −0.15, 0.31 m/s; Middle vs. Free p = 0.6896, 95% CI: −0.28, 0.19 m/s).

3.5. Uniaxial tensile testing

The tensile testing results closely mirrored patterns found in OCE. Overall, the elastic modulus of the AL was significantly greater than that of the PL (Anterior: 27.22 ± 20.44 MPa, Posterior: 10.49 ± 6.24 MPa, p = 0.0009, 95% CI: 8.92, 23.56 MPa; Fig. 5A). Similar to OCE, when comparing specific regions between the leaflets, the elastic modulus of the annular region of the AL was significantly greater than that of the PL (Anterior: 46.13 ± 20.49 MPa,

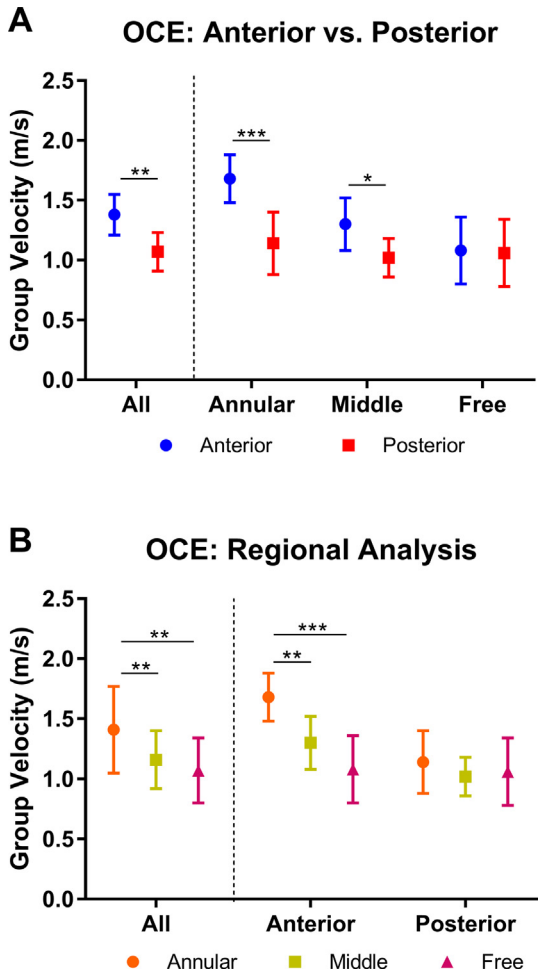

Fig. 4. (A) OCE analysis showed the anterior leaflet had a significantly greater group velocity than the posterior leaflet overall and specifically in the annular and middle regions. (B) The annular region had a significantly greater group velocity than both the middle and free regions overall and in the anterior leaflet independently. * = p < 0.05; ** = p < 0.01; *** = p < 0.001.

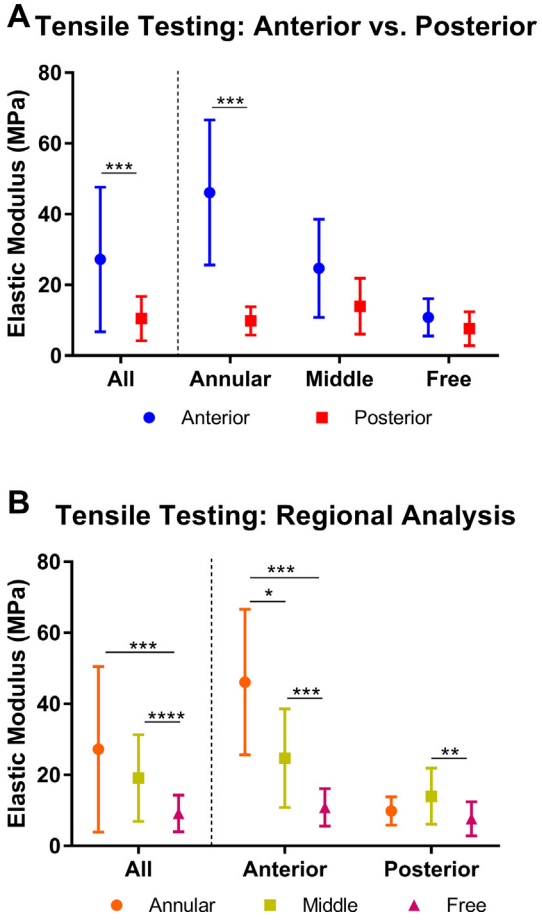

Fig. 5. (A) Tensile testing showed the anterior leaflet had a significantly greater elastic modulus than the posterior leaflet overall and specifically in the annular region. (B) A statistically significant gradient was detected in the elastic modulus between annular, middle, and free edge overall and in the anterior leaflet independently. * = p < 0.05; ** = p < 0.01; *** = p < 0.001; **** = p < 0.0001.

Posterior: 9.86 ± 4.00 MPa, p = 0.0003, 95% CI: 17.75, 54.18 MPa). There were no significant differences between the leaflets at the middle or free edge (Middle Anterior: 24.71 ± 13.88 MPa, Middle Posterior: 13.99 ± 7.89 MPa, p = 0.0392, 95% CI: −1.41, 21.78 MPa; Free Edge Anterior: 10.81 ± 5.27 MPa, Free Edge Posterior: 7.63 ± 4.79 MPa, p = 0.0947, 95% CI: −1.20, 6.37 MPa). Analysis of overall regional differences revealed both annular and middle regions had significantly greater elastic moduli than the free edge (Annular: 27.21 ± 23.28 MPa, Middle: 19.12 ± 12.19 MPa, p = 0.0770, 95% CI: −1.98, 19.05 MPa; Free Edge: 9.15 ± 5.17 MPa, p = 0.0008, 95% CI: −8.40, 38.63 MPa; Middle vs. Free Edge: p < 0.0001, 95% CI: 5.80, 14.40 MPa; Fig. 5B). In the AL, there were significant differences between each set of regions (Annular: 46.13 ± 20.49 MPa, Middle: 24.71 ± 13.88 MPa, p = 0.0128, 95% CI: 5.18, 37.66 MPa; Free Edge: 10.81 ± 5.27 MPa, p = 0.0002, 95% CI: 18.85, 49.85 MPa; Middle vs. Free Edge p = 0.0007, 95% CI: 7.33, 20.46 MPa). The PL, however, only showed a significant difference when comparing the middle and free edge (Annular: 9.86 ± 4.00 MPa, Middle: 13.99 ± 7.89 MPa, p = 0.0791, 95% CI: −9.47, 0.75 MPa; Free Edge: 7.63 ± 4.79 MPa, p = 0.2943, 95% CI: −22.48,−2.47 MPa; Middle vs Free Edge: p = 0.0083, 95% CI: 1.89,10.71 MPa).

4. Discussion

In this study, we have utilized OCE to map the velocity of an elastic wave in the MV at 1 mm increments along the radial length of the leaflets. Previous studies have established air-pulse OCE as a method for measuring the micro-scale differences in elastic behavior of various tissues *in situ* (Larin and Sampson, 2017). Here, we use a similar approach to investigate the highly heterogeneous environment of the MV and to better understand the material gradient along the leaflets. Using OCE, we found significant differences in elastic wave group velocity between leaflets and across regions within each leaflet. We additionally verified the pattern of these results by comparison with those from well-established tensile testing methods. This study serves as an initial validation of OCE in the study of MV mechanics. Future work will focus on the development of probe-based OCE, which will allow a cardiologist or cardiac surgeon to detect local regions of diseased, remodeled tissue in the MV for targeted repair *in vivo* (Karpiouk et al., 2018). An OCE probe may also be used to evaluate the efficacy of valve repair techniques, similar to force measurements and dimensional analysis that have previously been conducted *in vivo* and *in vitro* post-repair (Jensen et al., 2014, 2012; Siefert et al., 2014). This novel technology sheds light on mechanical differences between and within the leaflets and may lead to targeted regional therapies with better long-term outcomes for sufferers of MV disease.

OCE results showed the AL has a greater group velocity than the PL overall and specifically at the annular and middle regions. These patterns were verified using uniaxial testing and are consistent with previous reports of the relationship between the two leaflets using other testing methods (Connell et al., 2018; May-Newman and Yin, 1995; Stephens et al., 2010). However, unlike previous studies, this paper offers a direct point-by-point comparison along the entire radial length of the leaflets. Analyzing the spatial variation along the length of each leaflet, we found that the OCE measured significantly higher values of elastic wave group velocity at the annular edge compared to the middle and free edge. This result corroborates previous work that used an inverse finite element analysis to explore the spatial variation in the elastic modulus of ovine MV ALs (Krishnamurthy et al., 2009).

Taken together, our findings of high annular region elastic wave group velocity in the AL and the gradient in group velocity between the annular edge and the free edge are consistent with the leaflet composition. The AL clear zone at the annular edge is composed predominantly of a thick fibrosa layer with circumferentially-aligned collagen fibers, which bear the tensile load during valve opening. In contrast, the rough zone near the free edge contains less collagen and has a thicker spongiosa layer with a greater proportion of GAGs/PGs, which provide compressive strength during valve closing (Fig. 3C) (Grande-Allen and Liao, 2011). It has also been shown that the thick collagen-rich chordae in the AL rough zone, as well as in the PL, provide support at their insertion points, thus compensating for the relatively weaker mechanical behavior in these regions (Kunzelman and Cochran, 1992; May-Newman and Yin, 1995). The greater elastic wave group velocity of the annular region is also explained by the forces that it experiences; this region of the AL is primarily stationary during the cardiac cycle and therefore experiences a majority of the stress applied to the valve (Kunzelman et al., 2007; Sacks et al., 2006). This micro-scale study is the first to use OCE to map out the elastic properties of the MV along its radial length, providing insight into how known differences in the mitral composition are reflected by changing material properties. These findings are particularly notable since measurements were acquired with the chordal-side up, an orientation in which the collagen-rich fibrosa could easily have dampened the effects of the GAG/PG-rich spongiosa underneath. The detection of a significant gradient from annular edge to free edge speaks to OCE's ability to measure elastic properties through the depth of samples, as well as its utility in characterizing mechanical properties of layered tissue.

While our results are promising, certain limitations should be noted. The MV is a very active tissue *in vivo* and undergoes large stresses and strains that are not reproduced in this analysis. Therefore, the elastic properties acquired with OCE are orders of magnitude less than those measured by uniaxial tensile testing due to the nonlinear stress-strain curve of the leaflets and the higher level of strain in tensile testing (May-Newman and Yin, 1995). The OCE results more closely resemble those acquired using surface indentation techniques and can only be compared to other studies in terms of trends. The issue of scale in elastography is notable, as measurements at different scales (e.g., mm-scale versus nm-scale) measure the biomechanical properties of various tissue components (e.g., extracellular matrix versus collagen fibrils). Nonetheless, OCE offers advantages over nanoindentation, such as measuring at a larger scale (meso-scale) and providing high-resolution 3D images of the tissue being measured. One step of our future work is to perform the OCE measurements at various degrees of valve stretch, which may help corroborate the OCE measurements with tensile testing measurements. Because the limited frequency content of the elastic wave also limits spatial resolution, higher frequency excitation techniques are under development. Additionally, while the MV is highly anisotropic, we only measured the wave velocity along the circumferential direction. Measuring the MV's anisotropic biomechanical properties using OCE, as we have previously done in cornea, is a focus of our future work (Singh et al., 2017, 2016). Further, patterns in tissue anisotropy obtained by OCE could be verified using small angle light scattering or finite element analysis, which are both methods of measuring anisotropy that would offer more precise corroboration of OCE patterns than possible with tensile testing alone (Pant et al., 2018; Raghupathy and Barocas, 2010). Moreover, we are currently developing a layered model of the wave propagation that will provide quantitative material parameters and account for the agar basement. Hence, only the group velocity was reported here. Another step of our future work is to implement compression-based OCE to obtain the depth-wise heterogeneity of the heart valves, which has superior spatial elastographic resolution (Kennedy et al., 2015).

An initial goal of this study was to compare spatial variation between age groups to assess how group velocity patterns changed

with age. Previous studies from our lab have shown valve stiffness increases with age due to changes in valve layer composition, including increasing collagen cross-linking and changes in GAG/PG content (Stephens et al., 2010, 2008; Stephens and Grande-Allen, 2007). However, the pigs we used did not show any significant differences using either testing method. The clearest explanation for this is that the ages we chose (6 months and 2 years old) were not distinct enough to exhibit the expected differences. The prior studies used 6 weeks, 6 months, and 6 years old pigs, but due to limitations of the commercial abattoir, we were unable to acquire these more extreme age groups at this time. Exploring spatial variation in more aged valves is of great interest for future studies.

In summary, we have quantified the spatial variation of elasticity in the MV using air-pulse OCE. Our results confirm previously reported leaflet and regional comparisons, while providing greater resolution to these elasticity patterns. The presented OCE methods may be useful for future noninvasive studies evaluating success of MV repair mechanisms in maintaining physiological tissue properties.

Acknowledgements

This work was supported by the National Science Foundation Graduate Research Fellowship Program 1842494 to DPV and National Institutes of Health grant R01HL130804 to KVL. The authors would like to acknowledge Dr. Susobahn Das and Ms. Raksha Raghunathan at the University of Houston for their aid with experimental procedures.

Declaration of Competing Interest

None of the authors have conflicts of interest to report.

Appendix A. Supplementary material

Supplementary data to this article can be found online at https://doi.org/10.1016/j.jbiomech.2019.06.015.

References

Barber, J.E., Kasper, F.K., Ratliff, N.B., Cosgrove, D.M., Griffin, B.P., Vesely, I., 2001. Mechanical properties of myxomatous mitral valves. J. Thorac. Cardiovasc. Surg. 122, 955–962. https://doi.org/10.1067/mtc.2001.117621.

Benjamin, E.J., Muntner, P., Alonso, A., Bittencourt, M.S., Callaway, C.W., Carson, A.P., Chamberlain, A.M., Chang, A.R., Cheng, S., Das, S.R., Delling, F.N., Djousse, L., Elkind, M.S.V., Ferguson, J.F., Fornage, M., Jordan, L.C., Khan, S.S., Kissela, B.M., Knutson, K.L., Kwan, T.W., Lackland, D.T., Lewis, T.T., Lichtman, J.H., Longenecker, C.T., Loop, M.S., Lutsey, P.L., Martin, S.S., Matsushita, K., Moran, A.E., Mussolino, M.E., O'Flaherty, M., Pandey, A., Perak, A.M., Rosamond, W.D., Roth, G.A., Sampson, U.K.A., Satou, G.M., Schroeder, E.B., Shah, S.H., Spartano, N. L., Stokes, A., Tirschwell, D.L., Tsao, C.W., Turakhia, M.P., VanWagner, L.B., Wilkins, J.T., Wong, S.S., Virani, S.S., and on behalf of the American Heart Association Council on Epidemiology and Prevention Statistics Committee and Stroke Statistics Subcommittee, 2019. Heart disease and stroke statistics—2019 update: a report from the American Heart Association. Circulation 139, e56–e528. https://doi.org/10.1161/CIR.0000000000000659.

Bouma, W., Aoki, C., Vergnat, M., Pouch, A.M., Sprinkle, S.R., Gillespie, M.J., Mariani, M.A., Jackson, B.M., Gorman, R.C., Gorman, J.H., 2015. Saddle-shaped annuloplasty improves leaflet coaptation in repair for ischemic mitral regurgitation. Ann. Thorac. Surg. 100, 1360–1366. https://doi.org/10.1016/j.athoracsur.2015.03.096.

Connell, P.S., Vekilov, D.P., Diaz, C.M., Kim, S.E., Grande-Allen, K.J., 2018. Eliminating regurgitation reduces fibrotic remodeling of functional mitral regurgitation conditioned valves. Ann. Biomed. Eng. 1–14. https://doi.org/10.1007/s10439-018-1987-9.

Fedak, P.W.M., McCarthy, P.M., Bonow, R.O., 2008. Evolving concepts and technologies in mitral valve repair. Circulation 117, 963–974. https://doi.org/10.1161/CIRCULATIONAHA.107.702035.

Gillinov, A.M., Cosgrove, D.M., Blackstone, E.H., Diaz, R., Arnold, J.H., Lytle, B.W., Smedira, N.G., Sabik, J.F., McCarthy, P.M., Loop, F.D., 1998. Durability of mitral valve repair for degenerative disease. J. Thorac. Cardiovasc. Surg. 116, 734–743. https://doi.org/10.1016/S0022-5223(98)00450-4.

Graff, K.F., 2012. Wave Motion in Elastic Solids. Dover Publications, New York.

Grande-Allen, K.J., Borowski, A.G., Troughton, R.W., Houghtaling, P.L., Dipaola, N.R., Moravec, C.S., Vesely, I., Griffin, B.P., 2005. Apparently normal mitral valves in patients with heart failure demonstrate biochemical and structural derangements: an extracellular matrix and echocardiographic study. J. Am. Coll. Cardiol. 45, 54–61. https://doi.org/10.1016/j.jacc.2004.06.079.

Grande-Allen, K.J., Liao, J., 2011. The heterogeneous biomechanics and mechanobiology of the mitral valve: implications for tissue engineering. Curr. Cardiol. Rep. 13, 113–120. https://doi.org/10.1007/s11886-010-0161-2.

Grashow, J.S., Yoganathan, A.P., Sacks, M.S., 2006. Biaixal stress-stretch behavior of the mitral valve anterior leaflet at physiologic strain rates. Ann. Biomed. Eng. 34, 315–325. https://doi.org/10.1007/s10439-005-9027-y.

Hinton, R.B., Yutzey, K.E., 2011. Heart valve structure and function in development and disease. Annu. Rev. Physiol. 73, 29–46. https://doi.org/10.1146/annurev-physiol-012110-142145.

Huang, D., Swanson, E.A., Lin, C.P., Schuman, J.S., Stinson, W.G., Chang, W., Hee, M.R., Flotte, T., Gregory, K., Puliafito, C.A., Fujimoto, J.G., 1991. Optical coherence tomography. Science (80-.) 254, 1178–1181. https://doi.org/10.1126/SCIENCE.1957169.

Jensen, A.S., Baandrup, U., Hasenkam, J.M., Kundu, T., Jørgensen, C.S, 2006. Distribution of the microelastic properties within the human anterior mitral leaflet. Ultrasound Med. Biol. 32, 1943–1948. https://doi.org/10.1016/j.ultrasmedbio.2006.06.011.

Jensen, M.O., Honge, J.L., Benediktsson, J.A., Siefert, A.W., Jensen, H., Yoganathan, A. P., Snow, T.K., Hasenkam, J.M., Nygaard, H., Nielsen, S.L., 2014. Mitral valve annular downsizing forces: implications for annuloplasty device development. J. Thorac. Cardiovasc. Surg. 148, 83–89. https://doi.org/10.1016/J.JTCVS.2013.07.045.

Jensen, M.O., Jensen, H., Langhoff Honge, J., Nygaard, H., Michael Hasenkam, J., Nielsen, S.L., 2012. External approach to in vivo force measurement on mitral valve traction suture. J. Biomech. 45, 908–912. https://doi.org/10.1016/j.jbiomech.2011.11.034.

Jensen, M.O., Jensen, H., Smerup, M., Levine, R.A., Yoganathan, A.P., Nygaard, H., Hasenkam, J.M., Nielsen, S.L., 2008. Saddle-shaped mitral valve annuloplasty rings experience lower forces compared with flat rings. Circulation 118, S250–S255. https://doi.org/10.1161/CIRCULATIONAHA.107.746776.

Karpiouk, A.B., VanderLaan, D.J., Larin, K.V., Emelianov, S.Y., 2018. Integrated optical coherence tomography and multielement ultrasound transducer probe for shear wave elasticity imaging of moving tissues. J. Biomed. Opt. 23, 1–7. https://doi.org/10.1117/1.JBO.23.10.105006.

Kennedy, K.M., Chin, L., McLaughlin, R.A., Latham, B., Saunders, C.M., Sampson, D.D., Kennedy, B.F., 2015. Quantitative micro-elastography: imaging of tissue elasticity using compression optical coherence elastography. Sci. Rep. 5, 15538. https://doi.org/10.1038/srep15538.

Koch, T.M., Reddy, B.D., Zilla, P., Franz, T., 2010. Aortic valve leaflet mechanical properties facilitate diastolic valve function. Comput. Methods Biomech. Biomed. Engin. 13, 225–234. https://doi.org/10.1080/10255840903120160.

Krishnamurthy, G., Itoh, A., Swanson, J.C., Bothe, W., Karlsson, M., Kuhl, E., Craig Miller, D., Ingels, N.B., 2009. Regional stiffening of the mitral valve anterior leaflet in the beating ovine heart. J. Biomech. 42, 2697–2701. https://doi.org/10.1016/j.jbiomech.2009.08.028.

Kunzelman, K., Einstein, D., Cochran, R., 2007. Fluid-structure interaction models of the mitral valve: function in normal and pathological states. Philos. Trans. R. Soc. B Biol. Sci. 362, 1393–1406. https://doi.org/10.1098/rstb.2007.2123.

Kunzelman, K.S., Cochran, R.P., 1992. Stress/strain characteristics of porcine mitral valve tissue: parallel versus perpendicular collagen orientation. J. Card. Surg. 7, 71–78. https://doi.org/10.1111/j.1540-8191.1992.tb00777.x.

Kunzelman, K.S., Cochran, R.P., Chuong, C., Ring, W.S., Verrier, E.D., Eberhart, R.D., 1993a. Finite element analysis of the mitral valve. J. Heart Valve Dis. 2, 326–340.

Kunzelman, K.S., Cochran, R.P., Murphree, S.S., Ring, W.S., Verrier, E.D., Eberhart, R. C., 1993b. Differential collagen distribution in the mitral valve and its influence on biomechanical behaviour. J. Heart Valve Dis. 2, 236–244.

Larin, K.V., Sampson, D.D., 2017. Optical coherence elastography – OCT at work in tissue biomechanics. Biomed. Opt. Express 8, 1172–1202. https://doi.org/10.1364/BOE.8.001172.

Manapuram, R.K., Manne, V.G.R., Larin, K.V., 2009. Phase-sensitive swept source optical coherence tomography for imaging and quantifying of microbubbles in clear and scattering media. J. Appl. Phys. 105,. https://doi.org/10.1063/1.3116614 102040.

Manapuram, R.K., Manne, V.G.R., Larin, K.V., 2008. Development of phase-stabilized swept-source OCT for the ultrasensitive quantification of microbubbles. Laser Phys. 18, 1080–1086. https://doi.org/10.1134/S1054660X08090144.

May-Newman, K., Yin, F.C., 1995. Biaxial mechanical behavior of excised porcine mitral valve leaflets. Am. J. Physiol. 269, H1319–H1327.

Pant, A.D., Thomas, V.S., Black, A.L., Verba, T., Lesicko, J.G., Amini, R., 2018. Pressure-induced microstructural changes in porcine tricuspid valve leaflets. Acta Biomater. 67, 248–258. https://doi.org/10.1016/J.ACTBIO.2017.11.040.

Pham, T., Sun, W., 2014. Material properties of aged human mitral valve leaflets. J. Biomed. Mater. Res. - Part A 102, 2692–2703. https://doi.org/10.1002/jbm.a.34939.

Puperi, D.S., 2016. Biomimetic heterogeneous scaffolds for a layered tissue engineered heart valve.

Rabbah, J.-P.M., Saikrishnan, N., Siefert, A.W., Santhanakrishnan, A., Yoganathan, A. P., 2013. Mechanics of healthy and functionally diseased mitral valves: a critical review. J. Biomech. Eng. 135,. https://doi.org/10.1115/1.4023238 021007.

Raghupathy, R., Barocas, V.H., 2010. Generalized anisotropic inverse mechanics for soft tissues. J. Biomech. Eng. 132,. https://doi.org/10.1115/1.4001257 081006.

Sacks, M.S., Enomoto, Y., Graybill, J.R., Merryman, W.D., Zeeshan, A., Yoganathan, A. P., Levy, R.J., Gorman, R.C., Gorman, J.H., 2006. In-vivo dynamic deformation of the mitral valve anterior leaflet. Ann. Thorac. Surg. 82, 1369–1377. https://doi.org/10.1016/j.athoracsur.2006.03.117.

Sacks, M.S., Yoganathan, A.P., 2007. Heart valve function: a biomechanical perspective. Philos. Trans. R. Soc. Lond. B. Biol. Sci. 362, 1369–1391. https://doi.org/10.1098/rstb.2007.2122.

Schmitt, J., 1998. OCT elastography: imaging microscopic deformation and strain of tissue. Opt. Express 3, 199–211.

Siefert, A.W., Rabbah, J.-P.M., Pierce, E.L., Kunzelman, K.S., Yoganathan, A.P., 2014. Quantitative evaluation of annuloplasty on mitral valve chordae tendineae forces to supplement surgical planning model development. Cardiovasc. Eng. Technol. 5, 35–43. https://doi.org/10.1007/s13239-014-0175-9.

Singh, M., Li, J., Han, Z., Raghunathan, R., Nair, A., Wu, C., Liu, C.-H., Aglyamov, S., Twa, M.D., Larin, K.V., 2017. Assessing the effects of riboflavin/UV-A crosslinking on porcine corneal mechanical anisotropy with optical coherence elastography. Biomed. Opt. Express 8, 349–366. https://doi.org/10.1364/BOE.8.000349.

Singh, M., Li, J., Han, Z., Wu, C., Aglyamov, S.R., Twa, M.D., Larin, K.V., 2016. Investigating elastic anisotropy of the porcine cornea as a function of intraocular pressure with optical coherence elastography. J. Refract. Surg. 32, 562–567. https://doi.org/10.3928/1081597X-20160520-01.

Song, S., Huang, Z., Wang, R.K., 2013. Tracking mechanical wave propagation within tissue using phase-sensitive optical coherence tomography: motion artifact and its compensation. J. Biomed. Opt. 18,. https://doi.org/10.1117/1.JBO.18.12.121505 121505.

Spiegelstein, D., Sternik, L., Orlov, B., Shinfeld, A., Feinberg, M.S., Malachy, A., Raanani, E., 2013. Mitral valve repair: isolated posterior compared to anterior or bileaflet Pathology. J. Card. Surg. 28, 89–96. https://doi.org/10.1111/jocs.12051.

Stephens, E.H., Chu, C.K., Grande-Allen, K.J., 2008. Valve proteoglycan content and glycosaminoglycan fine structure are unique to microstructure, mechanical load and age: relevance to an age-specific tissue-engineered heart valve. Acta Biomater. 4, 1148–1160. https://doi.org/10.1016/j.actbio.2008.03.014.

Stephens, E.H., de Jonge, N., McNeill, M.P., Durst, C.A., Grande-Allen, K.J., 2010. Age-related changes in material behavior of porcine mitral and aortic valves and correlation to matrix composition. Tissue Eng. Part A 16, 867–878.

Stephens, E.H., Grande-Allen, K.J., 2007. Age-related changes in collagen synthesis and turnover in porcine heart valves. J. Heart Valve Dis. 16, 672–682.

Wang, S., Larin, K.V., 2014. Shear wave imaging optical coherence tomography (SWI-OCT) for ocular tissue biomechanics. Opt. Lett. 39, 41–44.

Wang, S., Larin, K.V., Li, J., Vantipalli, S., Manapuram, R.K., Aglyamov, S., Emelianov, S., Twa, M.D., 2013. A focused air-pulse system for optical-coherence-tomography-based measurements of tissue elasticity. Laser Phys. Lett. 10,. https://doi.org/10.1088/1612-2011/10/7/075605 075605.